



# Direct Z-scheme $\text{g-C}_3\text{N}_4/\text{WO}_3$ photocatalyst with atomically defined junction for $\text{H}_2$ production

Weilai Yu<sup>a,d,\*</sup>, Junxiang Chen<sup>a</sup>, Tongtong Shang<sup>b</sup>, Linfeng Chen<sup>a</sup>, Lin Gu<sup>b,c,\*\*</sup>, Tianyou Peng<sup>a</sup>

<sup>a</sup> College of Chemistry and Molecular Sciences, Wuhan University, Wuhan 430072, China

<sup>b</sup> Beijing National Laboratory for Condensed Matter Physics, Collaborative Innovation Center of Quantum Matter, Institute of Physics, Chinese Academy of Sciences, Beijing 100190, China

<sup>c</sup> School of Physical Sciences, University of Chinese Academy of Sciences, Beijing 100190, China

<sup>d</sup> Division of Chemistry and Chemical Engineering, California Institute of Technology, Pasadena, CA 91125, USA



## ARTICLE INFO

### Article history:

Received 6 July 2017

Received in revised form 29 July 2017

Accepted 3 August 2017

Available online 8 August 2017

### Keywords:

Z-scheme

Internal electric field

Carbon nitride

Atomic structure

Photocatalytic  $\text{H}_2$  production

## ABSTRACT

Mimicking the natural photosynthesis, artificial Z-scheme photocatalysis enables more efficient utilization of solar energy for sustainable chemical fuel production. Herein, a direct Z-scheme  $\text{g-C}_3\text{N}_4/\text{WO}_3$  photocatalyst with host-guest architecture is rationally designed, demonstrating significantly enhanced activities of photocatalytic  $\text{H}_2$  production. Unprecedented atomic-scale imaging of both the in-plane and interlayer structures in  $\text{g-C}_3\text{N}_4$  revealed the well-defined interfaces in such architecture, where the 2D  $\text{g-C}_3\text{N}_4$  layers stand vertically on the flat facets of  $\text{WO}_3$  nanocuboids. Through both experimental and theoretical investigations, mechanistic insights regarding the direct Z-scheme electron transfer from  $\text{WO}_3$  to  $\text{g-C}_3\text{N}_4$  were obtained. The Z-scheme electron transfer was driven by the internal electric field at the interfacial junction, defined by the covalent  $\text{W}-\text{O}-\text{N}-(\text{C})_2$  interaction. Under simultaneous light excitation, this atomically defined junction induces a rapid electron injection from  $\text{WO}_3$  to inhibit the fast recombination kinetics within  $\text{g-C}_3\text{N}_4$  and prolong the charge carrier lifetime of  $\text{g-C}_3\text{N}_4$ , thereby liberating more excited electrons with high reducing power for  $\text{H}_2$  production.

© 2017 Elsevier B.V. All rights reserved.

## 1. Introduction

With increasing global energy demand, heterogenous photocatalysis is an effective approach for sustainable solar fuel production [1–3]. Since 1972 when Fujishima and Honda demonstrated the proof-of-concept study by devising a  $\text{TiO}_2/\text{Pt}$  photoelectrochemical cell, the solar-driven  $\text{H}_2$  production from water by semiconductor photocatalysts has gained dramatic attention worldwide [4–8]. At present, numerous photoactive semiconductor materials have been discovered for light energy harvesting [9,10]. However, the activity of single-phase semiconductor photocatalyst is greatly limited by its insufficient light absorption and fast recombination of charge carriers. Combining two semiconductors with suitable band alignment is a promising

strategy to yield an enhanced photocatalytic activity, by simultaneously extending light absorption and promoting charge separation [11–14]. Conventional heterojunctions typically result in unfavorable losses of redox ability for photogenerated charge carriers. On the contrary, upon simultaneous two-photon excitation, the dual-band Z-scheme photocatalysts that mimic the natural photosynthesis can maintain both the high reducing and oxidizing power of photogenerated charge carriers and thus elevate the overall utilization efficiency of solar energy [15–19]. Therefore, devising new Z-scheme photocatalytic systems by appropriately interfacing different semiconductor materials is highly desirable.

Graphitic carbon nitride ( $\text{g-C}_3\text{N}_4$ ), a stable and nontoxic polymeric semiconductor, was introduced for photocatalytic water splitting under visible-light illumination [20–22]. Due to its narrow band gap (2.7 eV) and negative conduction band (CB) edge position (−1.1 V vs. NHE),  $\text{g-C}_3\text{N}_4$  is especially suitable to achieve photoinduced reactions of  $\text{H}_2$  generation and  $\text{CO}_2$  reduction [23–26]. Combining  $\text{g-C}_3\text{N}_4$  with inorganic semiconductors is a promising strategy to achieve spatial separation of charge carriers and enhanced photocatalytic performances [27–31]. Recently, we showed that the excited electrons in  $\text{g-C}_3\text{N}_4$  were more likely to

\* Corresponding author at: College of Chemistry and Molecular Sciences, Wuhan University, Wuhan 430072, China.

\*\* Corresponding author at: Beijing National Laboratory for Condensed Matter Physics, Collaborative Innovation Center of Quantum Matter, Institute of Physics, Chinese Academy of Sciences, Beijing 100190, China.

E-mail addresses: [yuweilai93@whu.edu.cn](mailto:yuweilai93@whu.edu.cn) (W. Yu), [l.gu@iphy.ac.cn](mailto:l.gu@iphy.ac.cn) (L. Gu).

recombine with its holes than interfacially transfer to other coupled inorganic semiconductors [29]. Thus, a full exploitation of the excited electrons in g-C<sub>3</sub>N<sub>4</sub> with high reducing power highly necessitates the fabrication of Z-scheme photocatalytic systems.

To realize this goal, a host-guest concept is rationally employed here by embedding the guest WO<sub>3</sub> nanocuboids in the host g-C<sub>3</sub>N<sub>4</sub> polymers to achieve materials integration with intimate interfacial contact [32–34]. The more positive band edges and the higher electron mobility of metal oxides are expected to concurrently enable a rapid electron injection into the valence band (VB) of g-C<sub>3</sub>N<sub>4</sub> under type-II band alignment, thereby greatly retarding the fast recombination kinetics of g-C<sub>3</sub>N<sub>4</sub> and promoting the photocatalytic performances. Although there are several previous reports on the enhanced photocatalytic performances of the g-C<sub>3</sub>N<sub>4</sub>/WO<sub>3</sub> composites, the underlying physical and structural factors responsible for the interfacial charge transfer have not been clearly identified [35–38]. Thus, it is clear that a combined study of experimental and theoretical investigations is highly necessary to provide deeper mechanistic insights towards more comprehensive understanding of this binary system. Moreover, similar band gaps of g-C<sub>3</sub>N<sub>4</sub> and WO<sub>3</sub> also make g-C<sub>3</sub>N<sub>4</sub>/WO<sub>3</sub> an almost ideal system to evaluate the charge separation efficiency and interfacial junction performances by maintaining nearly the same light absorption range and charge carrier generation rate.

In this work, we design such a host-guest architecture *via* partial intercalation of the WO<sub>3</sub> nanocuboids (guest) within g-C<sub>3</sub>N<sub>4</sub> (host) featuring their simultaneous exposure to light illumination. Despite the inactivity of WO<sub>3</sub> for direct photocatalytic H<sub>2</sub> production, the resulting g-C<sub>3</sub>N<sub>4</sub>/WO<sub>3</sub> composites all exhibited significantly enhanced photoactivities, compared with pure g-C<sub>3</sub>N<sub>4</sub>. With the aid of spherical aberration-corrected scanning transmission electron microscopy (STEM), the well-defined interfaces between g-C<sub>3</sub>N<sub>4</sub> and WO<sub>3</sub> were clearly resolved. Unprecedentedly, both the in-plane and interlayer structures of g-C<sub>3</sub>N<sub>4</sub> were directly imaged at atomic scale. Combined with investigations of the interfacial charge density migration and charge carrier effective masses, it is revealed that this significant enhancement of photocatalytic activity benefits from the direct Z-scheme electron transfer from WO<sub>3</sub> into g-C<sub>3</sub>N<sub>4</sub>, driven by their internal electric field at the atomically defined junction. The rapid electron injection from WO<sub>3</sub> into g-C<sub>3</sub>N<sub>4</sub> results in both slower recombination rate and prolonged lifetime of photogenerated charge carriers in the bulk g-C<sub>3</sub>N<sub>4</sub>. In this way, this Z-scheme host-guest architectural design enables more efficient utilization of the excited electrons in g-C<sub>3</sub>N<sub>4</sub> with high reducing power for photocatalytic H<sub>2</sub> generation.

## 2. Experimental

### 2.1. Material synthesis

All chemicals were of analytical grade and used without further purification.

#### 2.1.1. Synthesis of WO<sub>3</sub> nanocuboids

Sodium tungstate dihydrate (Na<sub>2</sub>WO<sub>4</sub>·2H<sub>2</sub>O) is used as the precursor of monoclinic WO<sub>3</sub> nanocuboids and lactic acid is adopted as the capping agent to control its size and morphology [39]. In a typical synthesis, 1.0 g sodium tungstate dihydrate was first dissolved in 50 mL deionized water under vigorous stirring for 15 min. Then 1 mL lactic acid was added dropwise into the above solution and then the original colorless transparent solution gradually turned into light yellow. After continuous stirring for another 15 min, the pH of the solution was adjusted to 1.0 by adding 3 M HCl solution dropwise. Then the solution gradually turned into yellow gel type mixture and an additional 20 min stirring was given to ensure the

homogeneity of the solution. The resulting mixture was then transferred to a 80 mL Teflon-lined stainless steel autoclave. After the autoclave was tightly sealed, it was put into the oven for reaction at 180 °C for 24 h. A blue suspension was obtained afterwards and water and ethanol were used alternatively to remove the residues in the obtained products. The final products were collected by intense centrifugation and turned into yellow after drying in oven at 80 °C overnight. The XRD results confirmed that the final products were monoclinic WO<sub>3</sub> formed by the hydrolysis of tungstate anions under acidic environment.

#### 2.1.2. Synthesis of host/guest g-C<sub>3</sub>N<sub>4</sub>/WO<sub>3</sub> nano-architecture

2.40 g of melamine and a specific amount (*x* mg) of the as-prepared WO<sub>3</sub> nanocuboids were put into a crucible. The above solids were uniformly mixed in 20 mL ethanol and dispersed to form a suspension under vigorous stirring for 30 min. Then the crucible was put in the oven at 80 °C to remove the ethanol. Due to the low surface tension of ethanol, a light yellow solid mixture with smooth surface was then deposited at the bottom of crucible. Afterwards, the crucible was put into muffle furnace and was heated to 550 °C for 2 h with a heating-up time of 1 h. When cooled to room temperature, the obtained solid was ground to fine powder. Because of the same amount of melamine used in the syntheses of various samples, the resulting g-C<sub>3</sub>N<sub>4</sub>/WO<sub>3</sub> composites were labelled as GW<sub>x</sub>, where *x* indicated that *x* mg of the WO<sub>3</sub> nanocuboid was mixed with melamine. For the purpose of comparison, both pure g-C<sub>3</sub>N<sub>4</sub> and WO<sub>3</sub> were also prepared *via* the same synthetic route.

## 2.2. Characterization

X-ray diffraction (XRD) patterns were recorded on a D/Max-RB X-ray diffractometer (Rigaku, Japan) under Cu K $\alpha$  radiation at a scan rate ( $2\theta$ ) of 0.05° s<sup>-1</sup>. The accelerating voltage and applied current were 40 kV and 80 mA, respectively. Thermogravimetric analysis (TGA) of all samples was performed on a DTG-60H analyzer (Shimadzu Corp., Tokyo, Japan) to investigate their thermal properties. The temperature was heated from ambient to 900 °C at a rate of 10 °C min<sup>-1</sup>, using around 5 mg of each sample. UV-vis absorbance spectra were obtained on a UV-vis spectrophotometer (UV-2550, SHIMADZU, Japan) using die-pressed disk samples, in which BaSO<sub>4</sub> was used as the reflectance standard. Fourier transform infrared (FT-IR) spectra of the samples were recorded on an IR Affinity-1 FT-IR spectrometer, using conventional KBr pellets in the range of 4000–500 cm<sup>-1</sup> at room temperature. The solid-state NMR experiments were carried out at 11.7 T on a Bruker-500 spectrometer using the <sup>1</sup>H → <sup>13</sup>C CP/MAS NMR technique with the MAS spinning speed of 10 kHz, equipped with a double-resonance 4 mm probe. The  $\pi/2$  pulse length for <sup>1</sup>H was 4.1  $\mu$ s, the contact time was 5.5 ms, and the repetition time is 7.0 s. The chemical shifts were referenced HMB for <sup>13</sup>C. Field-emission scanning electron microscopy (FE-SEM) images and energy-dispersive X-ray (EDX) mapping profiles were obtained on a JSM-7500F scanning electron microscope (JEOL, Japan). Transmission electron microscopy (TEM) analyses were conducted on a Tecnai G<sup>2</sup> F20 S-TWIN microscope at an accelerating voltage of 200 kV. Spherical aberration-corrected scanning transmission electron microscopy (STEM) images were obtained using an ARM-200CF (JEOL, Japan) transmission electron microscope operating at 200 kV equipped with double spherical aberration (Cs) correctors. Nitrogen adsorption–desorption isotherms were measured on an ASAP 2020 nitrogen adsorption apparatus (Micromeritics, USA). All samples were degassed at 180 °C before measurements. The BET surface areas were determined by a multipoint BET method using the adsorption data in the relative pressure (P/P<sub>0</sub>) range of 0.05–0.25. The pore size distributions were determined using des-

orption data by the Barrett–Joyner–Halenda (BJH) method. X-ray photoelectron spectroscopy (XPS) measurements were obtained on an ultrahigh-vacuum VG ESCALAB 210 electron spectrometer equipped with a multi-channel detector. The spectrum was excited by Mg K $\alpha$  radiation of two anodes in the constant analyzer energy mode at 200 W. All the binding energies were referenced to the C 1s peak at 285.0 eV of the surface adventitious carbon. Photoluminescence (PL) emission spectra were measured on an F-7000 Fluorescence Spectrophotometer (Hitachi, Japan) at room temperature. The excitation wavelength is 315 nm, the scanning speed is 1200 nm min $^{-1}$  and the photomultiplier tube (PMT) voltage is 700 V. The width of both the excitation slit and the emission slit were 2.5 nm. Time-resolved transient photoluminescence decay profiles were obtained on a FLS920 fluorescence lifetime spectrophotometer (Edinburgh Instruments, UK). The time-dependent fluorescence curves were fitted through the bi-exponential model to calculate the shorter ( $\tau_1$ ) and longer ( $\tau_2$ ) lifetime [40,41].

### 2.3. Photocatalytic activity test

Photocatalytic H<sub>2</sub>-production reactions were performed in a 100 mL three-neck Pyrex flask at room temperature, with three openings of the flask sealed with rubber plugs. In a typical activity test, 50 mg of photocatalyst powder was uniformly suspended by ultra-sonication in 80 mL of aqueous solution containing 10 vol.% triethanolamine (TEOA) as sacrificial reagent. In order to photochemically deposit Pt co-catalyst onto the photocatalyst surface, 0.1 mL of H<sub>2</sub>PtCl<sub>6</sub>·6H<sub>2</sub>O aqueous solution (1 g/100 mL) was added into the suspension and the system was then exposed to a 300 W Xe arc lamp (Changzhou Siyu Science Co. Ltd., China) for 30 min of light irradiation. The reactant suspension was then bubbled with nitrogen gas for 30 min to ensure anaerobic environment. Next, 1 h of simulated solar irradiation was performed using the same 300 W Xe arc lamp under continuous stirring. 0.4 mL of gas was sampled by a microsyringe and the evolved hydrogen was evaluated by a gas chromatograph (GC-14C, Shimadzu, Japan) equipped with thermal conductive detector, 5 Å molecular sieve column and pure nitrogen as carrier gas. Cycled tests of photocatalytic H<sub>2</sub> production were performed by continuous sampling the gas products every one hour and re-bubbling the suspension with nitrogen gas for 30 min every three hours, without changing the original solutions of sacrificial reagents.

### 2.4. Photoelectrochemical measurements

Photoelectrochemical measurements were performed on a CHI 660D electrochemical workstation (Chenhua Instrument, Shanghai, China) in a conventional three-electrode configuration. The working electrode prepared with the sample has an active area of *ca.* 1 cm<sup>2</sup>. A Pt wire and a Ag/AgCl electrode were used as the counter and reference electrode, respectively. A low-power LED (3 W, 365 nm, Shenzhen LAMPLIC Science Co. Ltd. China) with an intensity of *ca.* 80.0 mW cm $^{-2}$  was used as the light source. 0.5 M Na<sub>2</sub>SO<sub>4</sub> aqueous solution was used as the electrolyte. Typically, the working electrodes were prepared as follows: 0.2 g of photocatalyst powder was mixed with 0.08 g of polyethylene glycol (molecular weight: 20,000) and 2 mL of ethanol. Then, the mixture was ground to form a slurry and the slurry was coated onto a pre-cleaned 2 cm × 1.2 cm F-doped SnO<sub>2</sub>-coated glass (FTO glass) electrode *via* a doctor blade technique. After drying, the prepared electrodes were calcined at 450 °C for 30 min in a muffle furnace, with a heating rate of 5 °C min $^{-1}$ .

### 2.5. DFT calculation

#### 2.5.1. Population analysis of g-C<sub>3</sub>N<sub>4</sub>/WO<sub>3</sub> interface

The g-C<sub>3</sub>N<sub>4</sub>/WO<sub>3</sub> interface was constructed by placing (C<sub>3</sub>N<sub>4</sub>)<sub>n</sub> above the WO<sub>3</sub> (200) surface based on the proposed chemical bonding pattern in Fig. 3i. Spin-polarized DFT calculations were performed with periodic super-cells under the generalized gradient approximation (GGA), using the Perdew–Burke–Ernzerhof (PBE) functional for exchange–correlation and the ultrasoft pseudopotentials for nuclei and core electrons. The Kohn–Sham orbitals were expanded in a plane-wave basis set with a kinetic energy cutoff of 30 Ry and the charge-density cutoff of 300 Ry. The Fermi-surface effects have been treated by the smearing technique of Methfessel and Paxton, using a smearing parameter of 0.02 Ry. Periodically repeated four-layer slabs structure were used to model the WO<sub>3</sub> (100) surface. The bottom two layers fixed to DFT-optimized equilibrium lattice constant of 14.7626 Å. The top two layers were allowed to relax with the adsorbates during the calculations until the Cartesian force components acting on each atom were below 10 $^{-3}$  Ry/Bohr and the total energy converged to within 10 $^{-5}$  Ry. A Slab of (2 × 2) is used and the Brillouin zones were sampled with a 4 × 4 × 1 k-point mesh. The PWSCF codes contained in the Quantum ESPRESSO distribution were used to implement most of the calculations [42].

#### 2.5.2. Calculation of charge carrier effective mass

The charge carrier effective masses of g-C<sub>3</sub>N<sub>4</sub> and WO<sub>3</sub> were investigated using first-principle DFT calculations based on a CASTEP code and the plane-wave pseudopotential method. The generalized gradient approximation (GGA) with Perdew–Burke–Ernzerhof (PBE) was used as the exchange–correlation function. The interaction between the ionic core and valence electrons was described by The ultrasoft pseudopotential. The lattice parameters and atomic coordinates were relaxed using a cutoff energy of 380 eV and Monkhorst–pack grids of 4 × 4 × 2 k-points for both g-C<sub>3</sub>N<sub>4</sub> and WO<sub>3</sub> models. Geometric optimization was first achieved using convergence thresholds of 2 × 10 $^{-5}$  eV per atom for total energy, 0.03 eV Å $^{-1}$  for maximum force, 0.05 GPa for pressure, and 0.001 Å for maximum displacement. The self-consistent calculations were performed with a total tolerance of less than 1 × 10 $^{-6}$  eV per atom. After geometric optimizations, the effective masses of charge carriers were calculated based on the obtained electronic band structures.

The charge carrier effective mass was calculated by parabolic fitting to the conduction band minimum (CBM) and valence band maximum (VBM) based on Eq. (1). Basically, the effective mass of a charge carrier is inversely proportional to its moving velocity according to Eq. (2), where  $v$  and  $m^*$  represent the transfer rate and effective mass of a charge carrier, respectively. Thus, a smaller value of charge carrier effective mass ( $m$ ) corresponds to a faster transfer rate.

$$m^* = \hbar^2 (d^2 E / dk^2)^{-1} \quad (1)$$

$$v = \hbar k / m^* \quad (2)$$

To evaluate the charge separation efficiency, the concept of relative effective mass ( $R$ ) was adopted based on Eq. (3). In general, a higher value of  $R$  means the higher separation tendency of photo-generated electron–hole pairs, resulting in slower recombination rate and better photocatalytic performance.

$$R = m^*_{\text{h}} / m^*_{\text{e}} \quad (3)$$

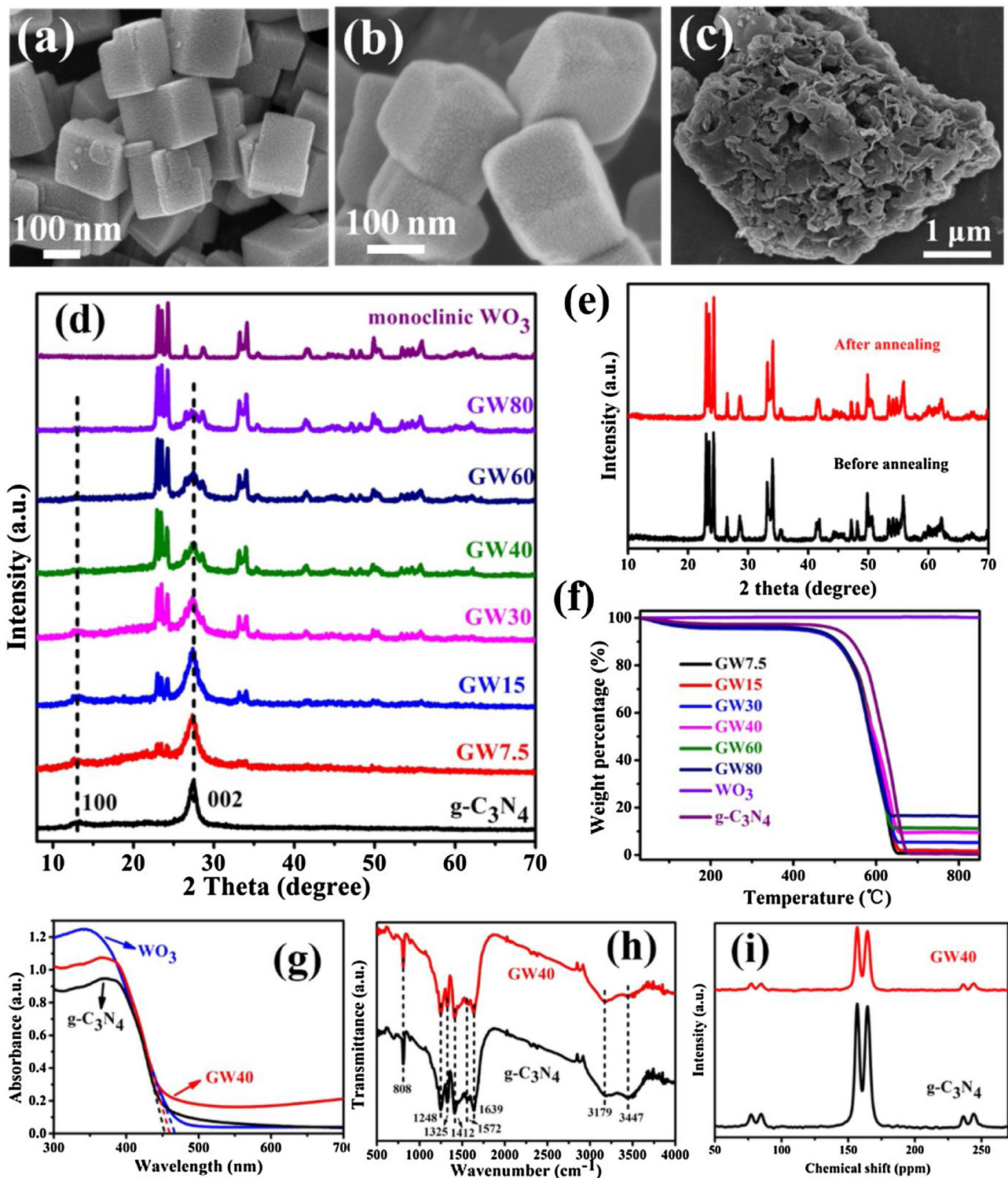


**Fig. 1.** (a–c) FE-SEM images of pristine WO<sub>3</sub> nanocuboids (a) before and (b) after annealing and (c) pure  $\text{g-C}_3\text{N}_4$ ; (d) XRD patterns for all the samples; (e) comparison of XRD patterns of pristine WO<sub>3</sub> before and after annealing; (f) TGA curves for all the samples; (g) UV-vis diffuse reflectance spectra (DRS) of pure  $\text{g-C}_3\text{N}_4$ , WO<sub>3</sub> and GW40; (h) FT-IR spectra of and (i) <sup>13</sup>C CP-MAS NMR spectra of pure  $\text{g-C}_3\text{N}_4$  and GW40 composite.

### 3. Results and discussions

Firstly, WO<sub>3</sub> nanocuboids were prepared via hydrothermal hydrolysis of tungstate anions using lactic acid as capping agent. These nanocuboids exhibited uniform sizes with length of 150–200 nm and generally exposed flat and smooth crystal facets with sharp edges as shown in Fig. 1a. The morphol-

ogy of WO<sub>3</sub> nanocuboids was largely maintained after annealing (Fig. 1b). Their edges grew smoother due to the surface roughening effect. Pure  $\text{g-C}_3\text{N}_4$  condensed from melamine showed large and compact microstructures whose extended length reached 5  $\mu\text{m}$  in Fig. 1c. Each individual microstructure was aggregated from densely packed lamellar structures demonstrating polymeric flexibility. The  $\text{g-C}_3\text{N}_4$ /WO<sub>3</sub> composites were fabricated via thermal

**Table 1**Weight content of  $\text{WO}_3$  in different  $\text{GW}_x$  composites.

Sample	$\text{WO}_3$ weight percentage/%
GW7.5	0.7
GW15	2
GW30	5.4
GW40	9.6
GW60	11.5
GW80	16.6

annealing of homogeneously mixed solids of melamine and the as-prepared  $\text{WO}_3$  nanocuboids. The resulting composites were labelled as  $\text{GW}_x$  according to the weight content of  $\text{WO}_3$ . The X-ray diffraction (XRD) patterns shown in Fig. 1d reveal that the pristine  $\text{WO}_3$  appears as the monoclinic phase. Moreover, the  $\text{WO}_3$  nanocuboids feature the exposed (200), (020) and (002) crystal facets with high and similar diffraction intensities [39]. No significant change of crystal phase was observed for pristine  $\text{WO}_3$  before and after annealing (Fig. 1e). The relative diffraction intensity of  $\text{WO}_3$  gradually increased with increasing ratio of  $\text{WO}_3$  in the composites. TGA analysis in Fig. 1f reveals a comparable thermal stability of  $\text{GW}_x$  composites as that of pure  $\text{g-C}_3\text{N}_4$ . More than 80% of the weight content in all the prepared  $\text{GW}_x$  samples refers to the bulk  $\text{g-C}_3\text{N}_4$  phase (Table 1). In this regard,  $\text{g-C}_3\text{N}_4$  in  $\text{GW}_x$  acts as a bulk host material residing the guest  $\text{WO}_3$  nanocuboids. The absorption edges of  $\text{g-C}_3\text{N}_4$  and  $\text{WO}_3$  were measured to be 450 and 470 nm by UV-vis DRS (Fig. 1g), corresponding to their intrinsic band gaps of 2.7 eV and 2.6 eV, respectively. This shows that  $\text{g-C}_3\text{N}_4$  and  $\text{WO}_3$  has similar band gaps and nearly the same range of light absorption. The increased light absorption of  $\text{GW40}$  sample at wavelength larger than 450 nm may be attributed to the defect states in  $\text{g-C}_3\text{N}_4$  due to the incorporation of  $\text{WO}_3$  nanocuboids during its polymerization [24]. Furthermore, the chemical structure of  $\text{g-C}_3\text{N}_4$  in  $\text{GW40}$  was proved to be the same as that of pure  $\text{g-C}_3\text{N}_4$  by both FT-IR spectra (Fig. 1h) and solid-state  $^{13}\text{C}$  NMR spectra (Fig. 1i). In the FT-IR spectra, the peaks at 1248, 1325 and 1412  $\text{cm}^{-1}$  are assigned to the aromatic C–N stretching, while the peaks at 1572 and 1639  $\text{cm}^{-1}$  are attributed to the C–N stretching vibration modes. The peaks at 808  $\text{cm}^{-1}$  belong to the out of plane bending modes of triazine units, indicating the presence of condensed C–N heterocycles. Moreover, the broad absorption bands at 3179 and 3447  $\text{cm}^{-1}$  are due to the adsorbed  $\text{H}_2\text{O}$  molecules and the N–H vibrations of the uncondensed amine groups [29]. For the solid-state  $^{13}\text{C}$  NMR measurements, the strong peaks at 156.8 and 164.5 ppm for both  $\text{GW40}$  and pure  $\text{g-C}_3\text{N}_4$  represent the C atoms in the mellem ( $\text{CN}_3$ ) and the C atoms connected to the tertiary N atoms within the tri-s-triazine units, respectively [43].

Fig. 2a–e demonstrates the typical morphology of  $\text{GW40}$  consisting of 9.6 wt.%  $\text{WO}_3$ . As seen in Fig. 2a, its bulk  $\text{g-C}_3\text{N}_4$  phase exhibited similar densely packed morphology as pure  $\text{g-C}_3\text{N}_4$ . The corresponding EDX mapping profiles revealed that the  $\text{WO}_3$  nanocuboids were dispersedly intercalated within the bulk  $\text{g-C}_3\text{N}_4$ . The enlarged view in Fig. 2b showed that the  $\text{WO}_3$  nanocuboids were actually partially wrapped within the  $\text{g-C}_3\text{N}_4$  microstructure. The distinct crystal edges of  $\text{WO}_3$  nanocuboids could be clearly identified, with flexible  $\text{g-C}_3\text{N}_4$  polymer attached onto their flat facets. Consistently, the TEM images in Fig. 2c, d confirmed that disperse distribution of  $\text{WO}_3$  nanocuboids within  $\text{g-C}_3\text{N}_4$ , forming an intimate interfacial contact. Structurally, the disperse existence and partial intercalation of  $\text{WO}_3$  nanostructures in the bulk  $\text{g-C}_3\text{N}_4$  can not only benefit their interfacial charge transfer but also maintain their simultaneous exposure to light illumination. Moreover, the HRTEM image and the SAED pattern reveal the single-crystalline nature of  $\text{WO}_3$  nanocuboids, ensuring its effective charge carrier transport at nanoscale towards the  $\text{g-C}_3\text{N}_4/\text{WO}_3$  interface (Fig. 2e, f) [44]. As denoted by dashed lines in Fig. 2c, some incompact grain

**Table 2**Specific surface area, pore volume and pore diameter of pristine  $\text{WO}_3$ ,  $\text{GW40}$  and  $\text{g-C}_3\text{N}_4$ .

Sample	$S_{\text{BET}}/\text{m}^2 \text{g}^{-1}$	$V_{\text{pore}}/\text{cm}^3 \text{g}^{-1}$	$d_{\text{pore}}/\text{nm}$
$\text{WO}_3$	3.3	0.01	10
$\text{GW40}$	34	0.16	19.2
$\text{g-C}_3\text{N}_4$	23	0.11	19.1

boundaries were also found in bulk  $\text{g-C}_3\text{N}_4$  according to the positions of intercalated  $\text{WO}_3$  nanocuboids. It can be estimated that the condensation of  $\text{g-C}_3\text{N}_4$  occurred based on the presence of  $\text{WO}_3$  nanocuboids and these imperfect areas suggest that the  $\text{g-C}_3\text{N}_4$  polymer could physically confluence during their extension from different  $\text{WO}_3$  nanocrystals. Compared with pure  $\text{g-C}_3\text{N}_4$ , the increased BET surface area and pore sizes of the  $\text{GW40}$  sample are also consistent with these observed imperfect and less compact regions within the  $\text{g-C}_3\text{N}_4/\text{WO}_3$  composite (Fig. 2g and Table 2).

To obtain insights into the structure of  $\text{g-C}_3\text{N}_4/\text{WO}_3$  interface, spherical aberration-corrected scanning transmission electron microscope (AC-STEM) images of  $\text{GW40}$  are shown in Fig. 3a, b. For the first time, both the in-plane and interlayer structure of  $\text{g-C}_3\text{N}_4$  were directly imaged at atomic scale. Fig. 3a reveals the annular bright field (ABF) imaging of the (100) in-plane structure of  $\text{g-C}_3\text{N}_4$  (top) connected with the  $\text{WO}_3$  lattice. The four-coordinated matrix at bottom is assigned to the (002) plane of monoclinic  $\text{WO}_3$ , where each dark spot refers to one heavy W atom inter-connected by lattice O atoms. Interestingly, the  $\text{g-C}_3\text{N}_4$  phase demonstrates as an assembly of regularly arranged triangular units with the same spatial orientation. Each of these triangular units is composed of three individual dark spots. Considering the extended network of tri-s-triazine units of  $\text{g-C}_3\text{N}_4$ , each triangular unit actually represents a tri-s-triazine unit ( $\text{C}_6\text{N}_7$ ), while each individual dark spot corresponds to a six-membered ring of triazine heterocycle ( $\text{C}_3\text{N}_3$ ). Owing to the electron delocalization in  $\pi$ – $\pi$  conjugated aromatic system, each  $\text{C}_3\text{N}_3$  triazine ring acts as one basic repeating unit with relatively large atomic number and reflects the in-plane periodicity of the  $\text{g-C}_3\text{N}_4$  crystal structure under STEM imaging. Similar phenomena were observed in other delocalized  $\pi$ – $\pi$  conjugated systems including graphene and carbon-doped boron nitride [45,46]. The tertiary nitrogen atoms cross-linking tri-s-triazine building blocks are not observed due to their very small atomic number. The same orientation of all triangular units gives a strong proof that the structure of  $\text{g-C}_3\text{N}_4$  should be assigned to the regularly extended tri-s-triazine network rather than a layered structure oppositely connected by linear melon chains [20,47]. Besides, each triangular unit was surrounded by six others, which was consistent with the spatial distribution of tri-s-triazine units in the extended network of  $\text{g-C}_3\text{N}_4$ . The inter-space between two neighboring triangular units was measured to be around 0.68 nm by Fast Fourier transform (FFT) analysis. This agreed well with the theoretical distance of (100) plane of  $\text{g-C}_3\text{N}_4$ , corresponding to the periodic distance between two adjacent tri-s-triazine units. More careful observation of the interfacial area between  $\text{g-C}_3\text{N}_4$  and  $\text{WO}_3$  shows that the triangular units of  $\text{g-C}_3\text{N}_4$  at the interface are unbroken, revealing the existence of complete tri-s-triazine units. More importantly, these tri-s-triazine units are well aligned with the lattice fringes of (200) plane of  $\text{WO}_3$  (solid lines). This perfect lattice alignment indicates the existence of well-defined W–O–N–(C) covalent bonds at interface. Fig. 3b exhibits the interlayer stacking of 2D planar structures of  $\text{g-C}_3\text{N}_4$  standing on the flat surface of  $\text{WO}_3$  nanocuboids under high angle annular dark-field (HAADF) imaging. The ABA periodic stacking pattern along the [002] crystal axis of  $\text{g-C}_3\text{N}_4$  could be clearly distinguished. Besides, the [002] crystal axis of  $\text{g-C}_3\text{N}_4$  is parallel to the  $\text{WO}_3$  surface, suggesting the vertical alignment of 2D layered  $\text{g-C}_3\text{N}_4$  on the flat facet of  $\text{WO}_3$ .

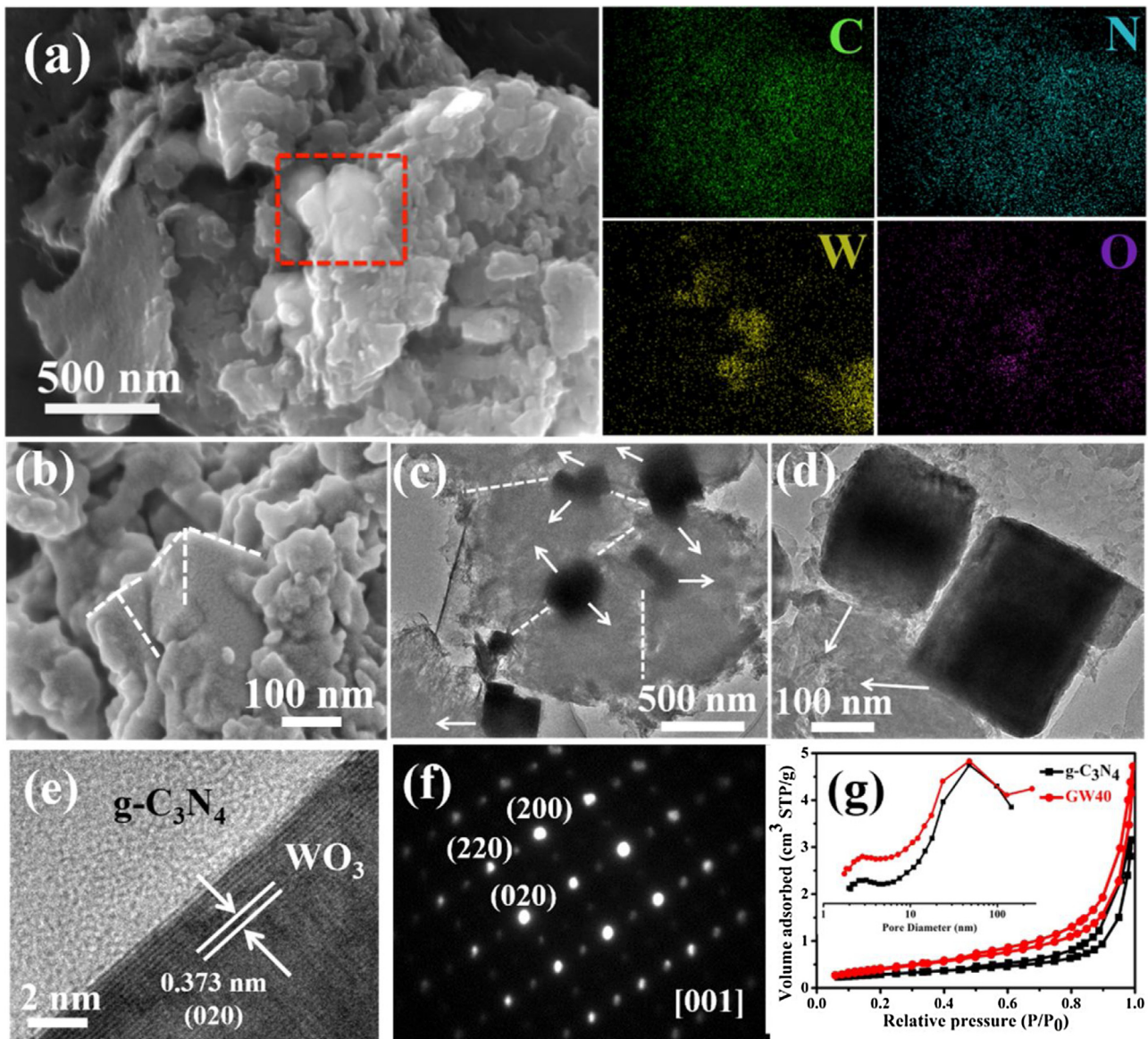


**Fig. 2.** (a) FE-SEM image of GW40 composite and its corresponding EDX mapping profiles; (b) an enlarged view of the selected area in (a) and the white dashed lines represent the identified  $\text{WO}_3$  crystal edges; (c, d) TEM images of GW40 composite; the white dashed lines and the arrows represent the incompact regions in bulk  $\text{g-C}_3\text{N}_4$  and its possible extension directions based on  $\text{WO}_3$  nanocuboids, respectively; (e) HR-TEM image of crystal lattice fringes of the (020) plane of  $\text{WO}_3$  nanocuboid with a distance of 0.373 nm and (f) its corresponding selected area electron diffraction (SAED) pattern; (g) nitrogen adsorption-desorption isotherms and pore size distributions (inset) of pure  $\text{g-C}_3\text{N}_4$  and GW40.

**Table 3**  
Calculated charge values of the N atoms in  $\text{g-C}_3\text{N}_4$  and the O atoms in  $\text{WO}_3$  before and after their interfacing. The gray, dark blue, red and light blue balls represent C, N, O, W atoms. The denoted N and O atoms are labelled with both yellow color and number.

Structures				
Atom number	$\text{g-C}_3\text{N}_4$	$\text{g-C}_3\text{N}_4@\text{WO}_3$	$\text{WO}_3$	$\text{WO}_3@\text{g-C}_3\text{N}_4$
1	5.25	5.20	6.15	6.18
2	5.26	5.20	6.16	6.17
3	5.17	5.11	6.16	6.18
4	–	–	6.16	6.19

nanocuboids. In this regard, the flat facets of  $\text{WO}_3$  nanocuboids are critical platforms to realize the direct atomic-scale imaging of  $\text{g-C}_3\text{N}_4$  structures.

To reveal the electron density migration at the  $\text{g-C}_3\text{N}_4/\text{WO}_3$  interface, high-resolution XPS spectra were obtained to elucidate the surface chemical states. Significant binding energy shifts are

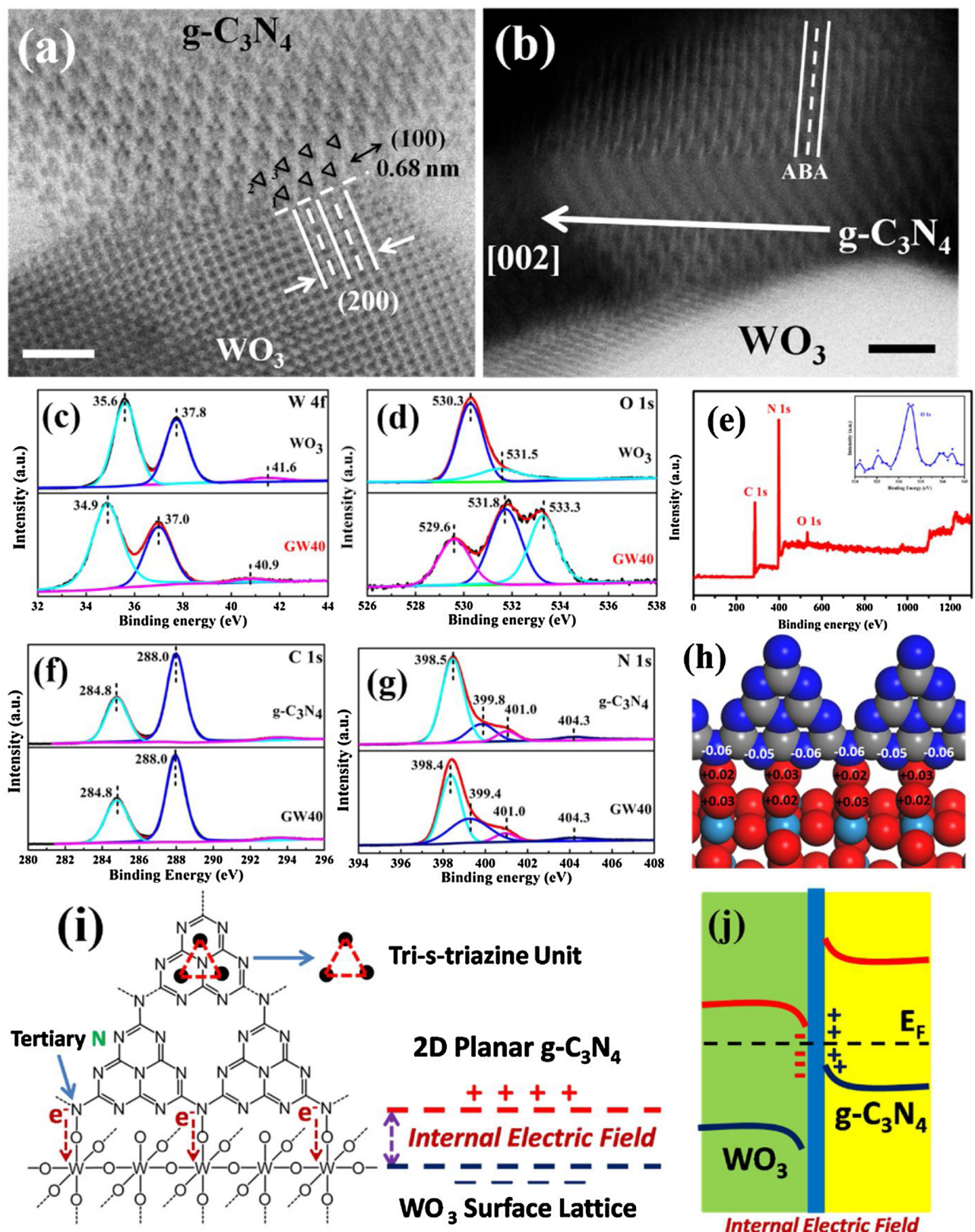


**Fig. 3.** (a, b) Spherical aberration-corrected STEM images of the well-defined interface between g-C<sub>3</sub>N<sub>4</sub> and WO<sub>3</sub> nanocuboids in GW40 composite, revealing both the (a) in-plane and (b) interlayer structure of g-C<sub>3</sub>N<sub>4</sub> (scale bars, 2 nm); (c, d) high-resolution XPS spectra of (c) W 4f and (d) O 1s; (e) XPS survey spectrum of pure g-C<sub>3</sub>N<sub>4</sub> and inset of its binding energy peak of O 1s state located at ca. 532–533 eV; (f, g) high-resolution XPS spectra of (f) C 1s and (g) N 1s; (h) the optimized structure of the g-C<sub>3</sub>N<sub>4</sub>/WO<sub>3</sub> interface with the change of electron density distribution, obtained by Lowdin charge analysis; the gray, dark blue, red and light blue balls represent the C, N, O and W atoms, respectively; the associated signed values (unit: e<sup>−</sup>) show that after structure optimization, the interfacial N and O atoms lose and gain electrons, respectively; (i) schematic illustration of the atomically defined junction at the g-C<sub>3</sub>N<sub>4</sub>/WO<sub>3</sub> interface and the internal electric field from g-C<sub>3</sub>N<sub>4</sub> (+) to WO<sub>3</sub> (−); (j) energy band diagram between WO<sub>3</sub> and g-C<sub>3</sub>N<sub>4</sub> with inverse band bending and internal electric field at interface. (For interpretation of the references to colour in this figure legend, the reader is referred to the web version of this article.)

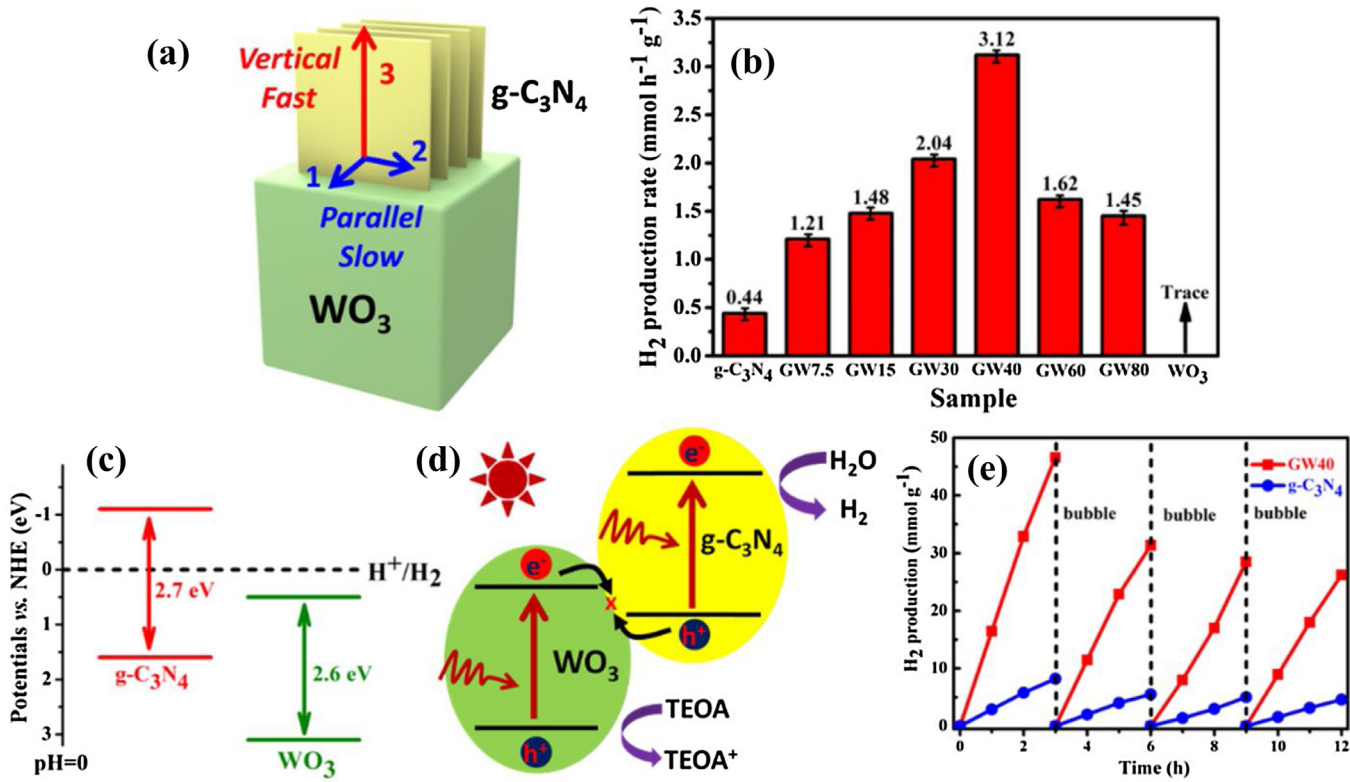


**Fig. 4.** (a) Schematic diagram of the growth and extension of  $\text{g-C}_3\text{N}_4$  in parallel (1 and 2, slow) and vertical (3, fast) direction to the flat surface of  $\text{WO}_3$  nanocuboids; (b) Comparison of average photocatalytic  $\text{H}_2$  production rates of  $\text{GW}_x$  composites and pure samples loaded with 1 wt.% Pt co-catalyst for the first three hours under simulated solar irradiation; (c) band energy diagram of the type-II band alignment between  $\text{g-C}_3\text{N}_4$  and  $\text{WO}_3$  in  $\text{GW}_x$  composites, in comparison to the NHE; (d) schematic diagram of the direct Z-scheme electron transfer from  $\text{WO}_3$  to  $\text{g-C}_3\text{N}_4$ ; (e) comparison of the cycled tests of photocatalytic  $\text{H}_2$  production for the  $\text{GW}_{40}$  sample and pure  $\text{g-C}_3\text{N}_4$ .

evident for both W 4f and O 1s states. The W 4f spectrum of pristine  $\text{WO}_3$  in Fig. 3c demonstrates two major peaks at 35.6 (W 4f<sub>7/2</sub>) and 37.8 eV (W 4f<sub>5/2</sub>), which can be assigned to the  $\text{W}^{6+}$  ions of  $\text{WO}_6$  octahedral in monoclinic  $\text{WO}_3$ . In contrast to pristine  $\text{WO}_3$ , all peaks of W states in  $\text{GW}_{40}$  are consistently shifted towards lower energy by 0.7–0.8 eV, indicating a decrease in the W oxidation state. The O 1s spectrum of pristine  $\text{WO}_3$  in Fig. 3d exhibits two peaks at 530.3 and 531.5 eV. The strong main peak at 530.3 eV can be attributed to the lattice O atoms of  $\text{WO}_3$ , while the weak shoulder peak at 531.5 eV can be assigned to the terminal hydroxyl groups (–OH) on surface. Three independent peaks at 529.6, 531.8 and 533.3 eV are found for the O 1s state of  $\text{GW}_{40}$ . The peaks at 531.8 and 533.3 eV are assigned to the oxygen atoms in  $\text{g-C}_3\text{N}_4$ , due to the oxidation effect during thermal condensation. This is consistent with the O 1s state found in the XPS survey spectrum (Fig. 3e) of pure  $\text{g-C}_3\text{N}_4$  at ca. 532–533 eV and the large oxygen-to-tungsten ratio (10.5) of  $\text{GW}_{40}$ . Thus, only the peak at 529.6 eV is ascribed to the  $\text{WO}_3$  phase, which is also shifted to lower energy by 0.7 eV as compared with pristine  $\text{WO}_3$ . In this regard, the significant decrease of binding energy for both W and O elements suggests that the total electron density increased in the  $\text{WO}_3$  phase of  $\text{GW}_{40}$  and this redundant electron density is shifted from  $\text{g-C}_3\text{N}_4$ . However, the C 1s and N 1s spectra of  $\text{GW}_{40}$  show negligible differences from those of pure  $\text{g-C}_3\text{N}_4$  (Fig. 3f, g). The absence of considerable binding energy shift for both C and N elements can be attributed to the large weight content and the giant sizes of  $\text{g-C}_3\text{N}_4$  in  $\text{GW}_{40}$ . Also, the ratio of its surface atoms in contact with  $\text{WO}_3$  nanocuboid can also be considered much smaller, compared with the much larger ratio of surface atoms for the nano-sized  $\text{WO}_3$  crystals. Thus, it is clear that the significant decrease of binding energy in  $\text{WO}_3$  indicated the electron density migration from  $\text{g-C}_3\text{N}_4$  to  $\text{WO}_3$ .

Based on the above STEM images, the chemical bonding pattern of the well-defined  $\text{g-C}_3\text{N}_4/\text{WO}_3$  interface was proposed in Fig. 3h, i. Each tertiary N atom linking two tri-s-triazine units of  $\text{g-C}_3\text{N}_4$  form covalent bonds with one dangling W–O bond on  $\text{WO}_3$  surface lattice. The flexibility of the surface dangling W–O bonds could compensate for the slight mismatch between the (100) plane of  $\text{g-C}_3\text{N}_4$  and the surface lattice of  $\text{WO}_3$ . Such interfacial covalent interaction forms an atomically defined junction and paves a direct pathway for electron transfer, thus greatly facilitating the spatial separation of charge carriers. Based on this proposed structure, theoretical DFT calculations of charge distribution at the structurally optimized  $\text{g-C}_3\text{N}_4/\text{WO}_3$  interface were also performed. Consistent with the XPS spectra, the calculated results confirm the existence of the electron density shift from  $\text{g-C}_3\text{N}_4$  to  $\text{WO}_3$  at ground state (Fig. 3h and Table 3). According to the energy band alignment between  $\text{g-C}_3\text{N}_4$  and  $\text{WO}_3$ , this migration of electron density is possible due to the different Fermi energy levels of  $\text{g-C}_3\text{N}_4$  (higher) and  $\text{WO}_3$  (lower). The equilibration of their different Fermi energy levels produces an internal electric field from  $\text{g-C}_3\text{N}_4$  (+) to  $\text{WO}_3$  (–) (Fig. 3i) and further drives the energy bands of  $\text{g-C}_3\text{N}_4$  and  $\text{WO}_3$  phase to bend up and down at their interface, respectively (Fig. 3j) [48]. Under simultaneous light excitation, the opposite band bending is expected to promote the recombination between the electrons in the CB of  $\text{WO}_3$  and the holes in the VB of  $\text{g-C}_3\text{N}_4$ , thus driving the direct Z-scheme charge transfer without the aid of any electron transfer mediator.

The presence of this well-defined interface again indicates that the condensation of melamine to form polymeric  $\text{g-C}_3\text{N}_4$  takes place in a modulated manner over the flat surface of  $\text{WO}_3$  nanocuboids. The dangling W–O bonds can serve as the active sites and first form covalent bonds with the tertiary N atoms of

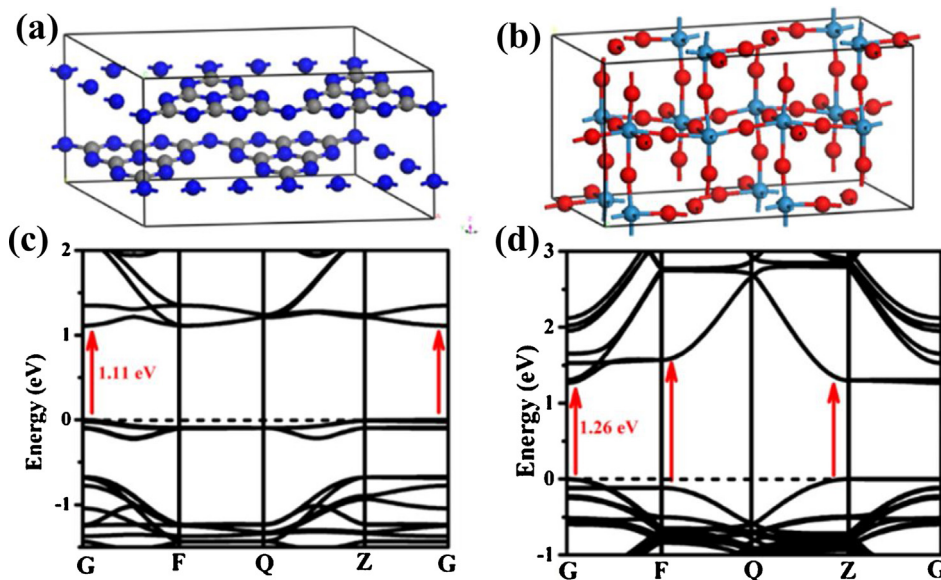


**Fig. 5.** (a, b) Crystals structures of (a)  $\text{g-C}_3\text{N}_4$  and (b) monoclinic  $\text{WO}_3$ ; the dark blue, gray, light blue and red balls represent N, C, W and O atoms, respectively; (c-d) the calculated electronic band structures of (c)  $\text{g-C}_3\text{N}_4$  and (d)  $\text{WO}_3$  based on the above crystal structures. (For interpretation of the references to colour in this figure legend, the reader is referred to the web version of this article.)

melamine. After initial polymerization of melamine,  $\text{g-C}_3\text{N}_4$  could further grow in three different directions: (a) interlayer stacking and (b) in-plane extension by aligning with the  $\text{WO}_3$  surface lattice and (c) unlimited vertical growth (Fig. 4a). Due to the regulations of simultaneous  $\text{WO}_3$  surface roughening and the required molecular conformation, both the parallel stacking and extension of  $\text{g-C}_3\text{N}_4$  along the interface are expected to occur in a much slower rate than its unlimited vertical growth. In this way, these vertically aligned 2D  $\text{g-C}_3\text{N}_4$  layers could undergo fast perpendicular growth and then self-organize into densely packed large microstructures. As a result, small  $\text{WO}_3$  nanocuboids were dispersedly embedded as guest within the surface regions of the host  $\text{g-C}_3\text{N}_4$  microparticles. Also, the physical confluence of  $\text{g-C}_3\text{N}_4$  grown from different  $\text{WO}_3$  nanocuboids formed many incompact areas observed in Fig. 2c. Owing to the different rates in parallel and vertical extension, the  $\text{WO}_3$  surface was only partly wrapped in  $\text{g-C}_3\text{N}_4$ , which is beneficial to achieve their simultaneous light excitation.

The photocatalytic  $\text{H}_2$ -production activity of samples was evaluated in 10 vol% TEOA aqueous solution under simulated solar irradiation. A comparison of the average photocatalytic  $\text{H}_2$  production rates is shown in Fig. 4b. After loading 1 wt.% Pt co-catalyst, pure  $\text{g-C}_3\text{N}_4$  only exhibited a moderate rate of photocatalytic  $\text{H}_2$  production ( $0.44 \text{ mmol h}^{-1} \text{ g}^{-1}$ ). Pristine  $\text{WO}_3$  nanocuboids failed to show any appreciable photocatalytic  $\text{H}_2$ -production activity. This was due to its more positive CB edge position (ca. 0.3 V vs. NHE) than the standard potential of  $\text{H}^+/\text{H}_2$  redox couple (Fig. 4c) [49]. Thus, only the excited electrons from the CB of  $\text{g-C}_3\text{N}_4$  (ca. -1.1 V vs. NHE) have enough reducing power for the  $\text{H}_2$  production reaction. However, when embedding a small amount of inactive  $\text{WO}_3$  nanocuboids into  $\text{g-C}_3\text{N}_4$ , all the fabricated GWx composites exhibited significantly enhanced activities in contrast to pure  $\text{g-C}_3\text{N}_4$ . Especially, GW40 exhibited the highest  $\text{H}_2$  production rate ( $3.12 \text{ mmol h}^{-1} \text{ g}^{-1}$ ), which is 7 times higher than that of pure  $\text{g-C}_3\text{N}_4$ . By comparing the band edge positions of  $\text{g-C}_3\text{N}_4$  and  $\text{WO}_3$ , the dramatic enhancement of photocatalytic activity of GWx composites was attributed to a direct Z-scheme mechanism in Fig. 4d. Under simultaneous light excitation, the excited electrons in the CB of  $\text{WO}_3$  undergo interfacial transfer to  $\text{g-C}_3\text{N}_4$  phase, subsequently quenching the photogenerated holes in the VB of  $\text{g-C}_3\text{N}_4$  (ca. 1.6 V vs. NHE). The internal electric field at the  $\text{g-C}_3\text{N}_4/\text{WO}_3$  interface

provided a driving force for such Z-scheme electron transfer to occur via the direct pathway paved by their host-guest covalent interaction. In this regard, both the internal electric field and the well-defined interface are critical for achieving the spatial separation of charge carriers.

The resulting activity of GWx composites varied according to the content of  $\text{WO}_3$ . The best performance of GW40 suggested an appropriate amount of  $\text{WO}_3$  was important to achieve the optimal activity of the final composites. Initially, increasing the amount of  $\text{WO}_3$  in the range of low weight ratio is favorable for increasing the interfacial covalent interaction between  $\text{g-C}_3\text{N}_4$  and  $\text{WO}_3$ , thus promoting charge transfer. However, the positive effect of interfacial charge separation could be deteriorated by the intrinsic inactivity of  $\text{WO}_3$  for  $\text{H}_2$  production. Thus, the overall activity of GWx composites gradually reaches a summit with increasing  $\text{WO}_3$  content, while further addition of  $\text{WO}_3$  caused an inevitable decrease of photoactivity. Excess amount of  $\text{WO}_3$  also increased the possibility of false loading of Pt co-catalyst on its inactive surface and induced inter-particle aggregation, which decreased interfacial contact and lowered photocatalytic performances. Also, it should be noted that the light absorption should remain similar in all the composite/pure samples, due to the similar band gaps of  $\text{g-C}_3\text{N}_4$  and  $\text{WO}_3$ . Thus, while having the nearly same charge carrier generation rates, the drastically enhanced activities of the  $\text{g-C}_3\text{N}_4/\text{WO}_3$  composites should be directly attributed to a much higher conversion efficiency from the photogenerated charge carriers to the final  $\text{H}_2$  products. The cycled tests of photocatalytic  $\text{H}_2$  production for the champion GW40 sample was shown in Fig. 4e. During the course of 12 h, the GW40 sample consistently demonstrated much higher  $\text{H}_2$  generation rates compared with pure  $\text{g-C}_3\text{N}_4$ . However, a trend of slight decrease was observed for the GW40 sample every time a new cycle was started. Since similar trend was also observed for pure  $\text{g-C}_3\text{N}_4$ , it might be due to the depletion effect of sacrificial reagents in the suspension system. Besides, the  $\text{H}_2$  evolving reaction itself may influence the structural stability and the overall performance of the Z-scheme  $\text{g-C}_3\text{N}_4/\text{WO}_3$  junction to some extent, considering that the  $\text{H}_2$  gas molecules are expected to bubble from the surface of the flexible  $\text{g-C}_3\text{N}_4$  polymer.

To support the above Z-scheme mechanism, theoretical DFT calculations of charge carrier effective mass were performed based

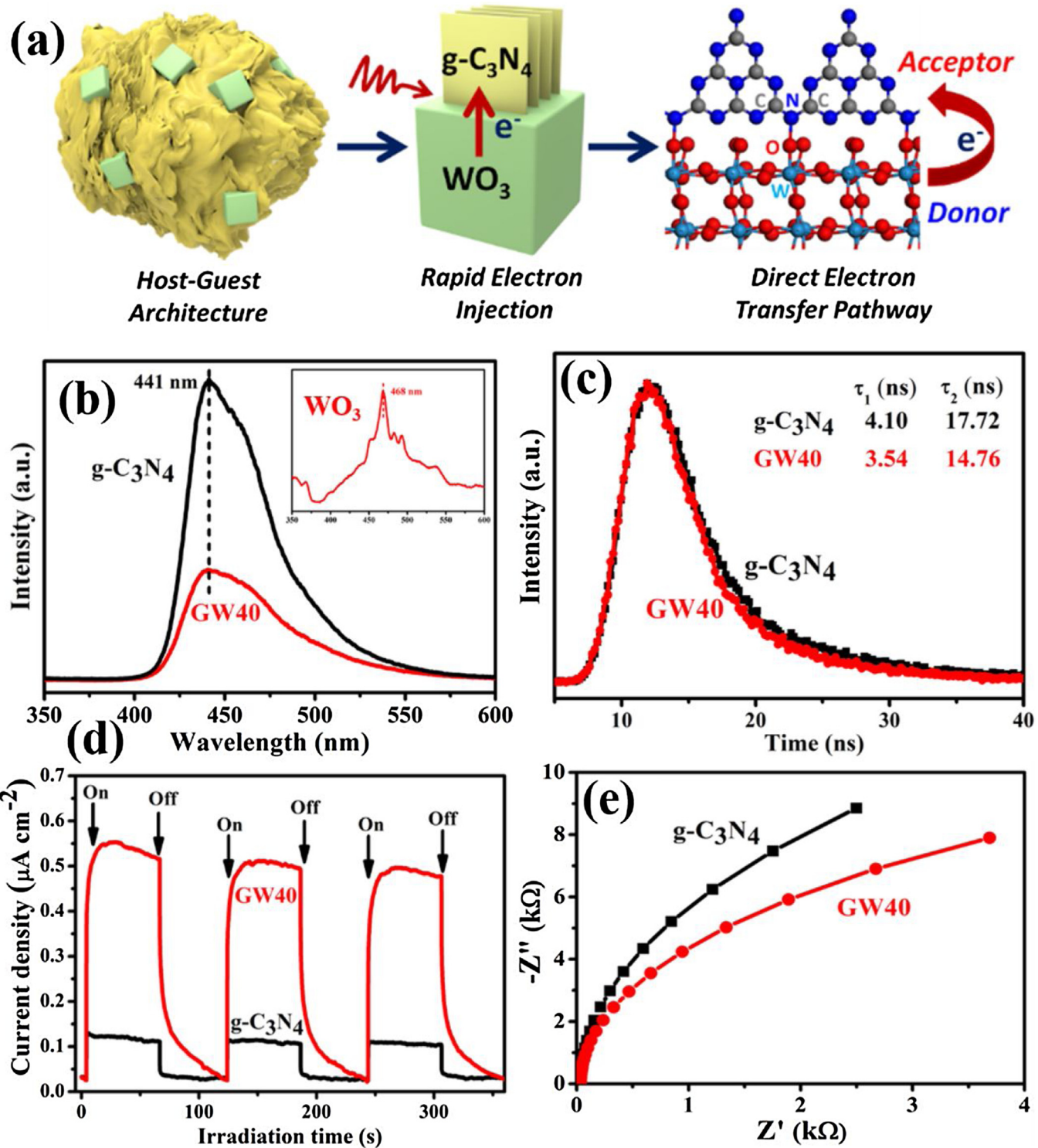


**Fig. 6.** (a) Schematic illustration of the function mechanism of  $\text{g-C}_3\text{N}_4/\text{WO}_3$  composites at multiple length scales; (b) PL spectra of pure  $\text{g-C}_3\text{N}_4$ , GW40 and pristine  $\text{WO}_3$  (inset); (c) time-resolved fluorescence decay profiles of pure  $\text{g-C}_3\text{N}_4$  and GW40 excited at the wavelength of 320 nm; (d) transient photocurrent response and (e) electrochemical impedance spectra of pure  $\text{g-C}_3\text{N}_4$  and GW40 in 0.5 M  $\text{Na}_2\text{SO}_4$  aqueous solution.

on the crystal structures and electronic band structures in Fig. 5 [50,51]. As an anisotropic property, the effective mass of charge carrier needs to be considered separately in different crystal directions. For  $\text{g-C}_3\text{N}_4$ , the calculated results in Table 4 show that its 2D in-plane structure produces much lighter photogenerated electrons ( $0.53 \text{ m}_0$ ) and holes ( $0.72 \text{ m}_0$ ), as compared with those electrons ( $1.8 \text{ m}_0$ ) and holes ( $71.0 \text{ m}_0$ ) travelling along its vertical direction

( $\text{c}$  axis) [52,53]. The fast mobility of charge carriers within the 2D plane of  $\text{g-C}_3\text{N}_4$  is attributed to the electron delocalization of  $\pi-\pi$  conjugation, while the slow charge carrier mobility along its vertical direction was due to the weak electronic coupling between the spatially separated 2D layers. Thus, most charge carriers of  $\text{g-C}_3\text{N}_4$  should migrate within 2D planes rather than travel through different layers. Recombination factor ( $R$ ) is defined as the ratio

**Table 4**

Calculated effective masses of charge carriers of  $g\text{-C}_3\text{N}_4$  along the designated crystal directions; unit for all the effective masses is  $m_0$ , the electron rest mass.

Direction	G-F	G-Z
$m_e^*$	0.53	1.8
$m_h^*$	0.72	71
R	1.3	39

**Table 5**

Calculated effective masses of charge carriers of monoclinic  $\text{WO}_3$  along the designated crystal directions; unit for all the effective masses is  $m_0$ , the electron rest mass.

Direction	G-F	F-Q	Z-Q
$m_e^*$	0.16	0.17	0.14
$m_h^*$	0.53	0.49	0.51
R	3.3	2.9	3.6

of the effective mass of hole to electron to evaluate the recombination rate of electron-hole pairs [54,55]. The small value of R for  $g\text{-C}_3\text{N}_4$  ( $R=1.3$ ) suggests that its fast recombination kinetics limits its photocatalytic performance. However, as shown in Table 5, monoclinic  $\text{WO}_3$  has not only much lighter charge carriers than those of  $g\text{-C}_3\text{N}_4$ , but also a slower recombination rate of photogenerated electron-hole pairs ( $R=2.9\text{--}3.6$ ). Compared with  $g\text{-C}_3\text{N}_4$ , the excited electrons of  $\text{WO}_3$  demonstrate a higher tendency to migrate from bulk to interface and then transfer into  $g\text{-C}_3\text{N}_4$ . In this regard, the interfacial electron transfer in  $\text{GW}_x$  is more likely to occur from  $\text{WO}_3$  to  $g\text{-C}_3\text{N}_4$ , which is consistent with the above direct Z-scheme mechanism.

The function mechanism of the  $g\text{-C}_3\text{N}_4/\text{WO}_3$  composites for enhanced photocatalytic  $\text{H}_2$  generation is demonstrated in Fig. 6a. A host-guest architecture in which the small  $\text{WO}_3$  nanocuboids were partially intercalated within the large  $g\text{-C}_3\text{N}_4$  microparticle leads to their simultaneous exposure to light excitation. After charge carrier generation, the higher electron mobility and slower charge recombination in  $\text{WO}_3$  directly injected a rapid flow of excited electrons from its CB (donor) into the VB of  $g\text{-C}_3\text{N}_4$  (acceptor). Besides, the standing morphology of  $g\text{-C}_3\text{N}_4$  layers on the exposed flat  $\text{WO}_3$  facets and their interfacial covalent interaction provided a straight pathway for the electron transfer from  $\text{WO}_3$  to  $g\text{-C}_3\text{N}_4$ , driven by the internal electric field at this atomically defined junction. This rapid electron injection quenched the photogenerated holes in  $g\text{-C}_3\text{N}_4$  and efficiently inhibited its recombination. It should be expected that the accelerated recombination between the electrons in the CB of  $\text{WO}_3$  and the holes in the VB of  $g\text{-C}_3\text{N}_4$  significantly prolongs the lifetime of excited electrons in  $g\text{-C}_3\text{N}_4$  and thus enables more excited electrons available for  $\text{H}_2$  production.

PL spectra were first obtained to evaluate the recombination rate of photogenerated electron-hole pairs (Fig. 6b). The PL spectra of pure  $g\text{-C}_3\text{N}_4$  and  $\text{GW}40$  have similar shapes, exhibiting emission peaks at 441 nm close to the absorption edge of  $g\text{-C}_3\text{N}_4$ . No obvious emission peak from  $\text{WO}_3$  is visible for  $\text{GW}40$ . Thus, the band-band PL phenomenon of  $g\text{-C}_3\text{N}_4$  is mainly responsible for the PL emission of  $\text{GW}40$ . The high PL intensity of pure  $g\text{-C}_3\text{N}_4$  was consistent with its fast recombination rate of photogenerated charge carriers. The much lower PL intensity of  $\text{GW}40$  indicates the recombination of charge carriers in bulk  $g\text{-C}_3\text{N}_4$  is greatly retarded by coupling with  $\text{WO}_3$ . Time-resolved fluorescence decay profiles of pure  $g\text{-C}_3\text{N}_4$  and  $\text{GW}40$  in Fig. 6c show that both the fast and slow components of the fluorescence lifetime in  $\text{GW}40$  ( $\tau_1=3.54\text{ ns}$ ,  $\tau_2=17.72\text{ ns}$ ) are shortened as compared with those of pure  $g\text{-C}_3\text{N}_4$  ( $\tau_1=4.10\text{ ns}$ ,  $\tau_2=14.76\text{ ns}$ ). Both the lower PL intensity and the decreased fluorescence lifetime of  $\text{GW}40$  strongly prove the presence of charge separation at the  $g\text{-C}_3\text{N}_4/\text{WO}_3$  interface.

Transient photocurrent responses were recorded by typical switch on-off cycles of light irradiation in Fig. 6d. The photocurrent response of  $\text{GW}40$  ( $0.48\text{ }\mu\text{A cm}^{-2}$ ) is 7 times higher than that of pure  $g\text{-C}_3\text{N}_4$  ( $0.07\text{ }\mu\text{A cm}^{-2}$ ). Under light illumination, the embedded  $\text{WO}_3$  nanocuboids promote the charge separation in  $\text{GW}_x$  composites via rapid injection of an electron flow. Both the low value of photocurrent and the quick decay character of pure  $g\text{-C}_3\text{N}_4$  can be assigned to its fast recombination kinetics. The much higher photocurrent of  $\text{GW}40$  suggests that the electron injection from  $\text{WO}_3$  to  $g\text{-C}_3\text{N}_4$  significantly slows down the recombination of charge carriers. Besides, the slower decay kinetics of  $\text{GW}40$  at turn-off of light irradiation indicates the prolonged lifetime of excited electrons of  $g\text{-C}_3\text{N}_4$  phase, consistent with more efficient separation of photogenerated electrons and holes. The electrochemical impedance spectra in Fig. 6e show that the  $\text{GW}40$  composite exhibited a reduced radius of Nyquist plot in contrast to that of pure  $g\text{-C}_3\text{N}_4$ . This implies that  $\text{GW}40$  composite has a smaller electronic resistance than that of pure  $g\text{-C}_3\text{N}_4$ , due to more effective charge transport and collection. All these above measurements confirm that the  $g\text{-C}_3\text{N}_4/\text{WO}_3$  composite produces more excited electrons with extended lifetime that are available for heterogeneous photocatalytic  $\text{H}_2$  production, again supporting the above direct Z-scheme mechanism.

#### 4. Conclusions

In summary, a direct Z-scheme host-guest  $g\text{-C}_3\text{N}_4/\text{WO}_3$  architecture was rationally constructed by partially embedding the guest  $\text{WO}_3$  nanocuboids into the host  $g\text{-C}_3\text{N}_4$ . The fabricated  $g\text{-C}_3\text{N}_4/\text{WO}_3$  composite all exhibited dramatically enhanced activities for photocatalytic  $\text{H}_2$  production. With the aid of spherical aberration-corrected STEM, the well-defined  $g\text{-C}_3\text{N}_4/\text{WO}_3$  interface was clearly resolved as the 2D  $g\text{-C}_3\text{N}_4$  layers standing vertically on the flat facets of  $\text{WO}_3$  nanocuboids. Unprecedentedly, both the in-plane and interlayer structures of  $g\text{-C}_3\text{N}_4$  were directly imaged at atomic scale. The internal electric field and the covalent W-O-N-(C)<sub>2</sub> interaction provides the driving force and the direct pathway, respectively, for achieving direct Z-scheme electron transfer from  $\text{WO}_3$  to  $g\text{-C}_3\text{N}_4$  at interface. Under simultaneous light excitation, this atomically defined junction induces a rapid electron injection from  $\text{WO}_3$  into  $g\text{-C}_3\text{N}_4$ . In this way, the fast recombination kinetics of  $g\text{-C}_3\text{N}_4$  is significantly inhibited and the lifetime of its charge carrier lifetime is also prolonged, thus liberating more excited electrons with high reducing power for  $\text{H}_2$  production. This work will provide new deep insights into the rational design of  $g\text{-C}_3\text{N}_4$ -based Z-scheme photocatalytic systems for more efficient solar energy utilization.

#### Acknowledgements

This work was supported by National Program on Key Basic Research Project (2014CB921002) and The Strategic Priority Research Program of Chinese Academy of Sciences (Grant No. XDB07030200) and National Natural Science Foundation of China (51522212, 51421002).

#### References

- [1] N.S. Lewis, D.G. Nocera, Powering the planet: chemical challenges in solar energy utilization, Proc. Natl. Acad. Sci. 103 (2006) 15729–15735.
- [2] D. Kim, K.K. Sakimoto, D. Hong, P. Yang, Artificial photosynthesis for sustainable fuel and chemical production, Angew. Chem. Int. Ed. 54 (2015) 3259–3266.
- [3] Q. Xiang, B. Cheng, J. Yu, Graphene-based photocatalysts for solar-fuel generation, Angew. Chem. Int. Ed. 54 (2015) 11350–11366.
- [4] A. Fujishima, K. Honda, Photolysis-decomposition of water at the surface of an irradiated semiconductor, Nature 238 (1972) 37–38.

[5] M.G. Walter, E.L. Warren, J.R. McKone, S.W. Boettcher, Q. Mi, E.A. Santori, N.S. Lewis, Solar water splitting cells, *Chem. Rev.* 110 (2010) 6446–6473.

[6] S. Cao, J. Yu, g-C<sub>3</sub>N<sub>4</sub>-based photocatalysts for hydrogen generation, *J. Phys. Chem. Lett.* 5 (2014) 2101–2107.

[7] X. Li, J. Yu, J. Low, Y. Fang, J. Xiao, X. Chen, Engineering heterogeneous semiconductors for solar water splitting, *J. Mater. Chem. A* 3 (2015) 2485–2534.

[8] D.M. Fabian, S. Hu, N. Singh, F.A. Houle, T. Hisatomi, K. Domen, F.E. Osterloh, S. Ardo, Particle suspension reactors and materials for solar-driven water splitting, *Energy Environ. Sci.* 8 (2015) 2825–2850.

[9] Q. Li, X. Li, S. Wageh, A.A. Al-Ghamdi, J. Yu, CdS/graphene nanocomposite photocatalysts, *Adv. Energy Mater.* 5 (2015) 1500010.

[10] L. Mu, Y. Zhao, A. Li, S. Wang, Z. Wang, J. Yang, Y. Wang, T. Liu, R. Chen, J. Zhu, F. Fan, R. Li, C. Li, Enhancing charge separation on high symmetry SrTiO<sub>3</sub> exposed with anisotropic facets for photocatalytic water splitting, *Energy Environ. Sci.* 9 (2016) 2463–2469.

[11] C. Liu, J. Tang, H.M. Chen, B. Liu, P. Yang, A fully integrated nanosystem of semiconductor nanowires for direct solar water splitting, *Nano Lett.* 13 (2013) 2989–2992.

[12] M.R. Shaner, K.T. Fountaine, S. Ardo, R.H. Coridan, H.A. Atwater, N.S. Lewis, Photoelectrochemistry of core-shell tandem junction n-p<sup>+</sup>-Si/n-WO<sub>3</sub> microwire array photoelectrodes, *Energy Environ. Sci.* 7 (2014) 779–790.

[13] J. Resasco, H. Zhang, N. Kornienko, N. Becknell, H. Lee, J. Guo, A.L. Briseno, P. Yang, TiO<sub>2</sub>/BiVO<sub>4</sub> nanowire heterostructure photoanodes based on type II band alignment, *ACS Cent. Sci.* 2 (2016) 80–88.

[14] J. Low, J. Yu, M. Jaroniec, S. Wageh, A.A. Al-Ghamdi, Heterojunction photocatalysts, *Adv. Mater.* 29 (2017) 1601694.

[15] P. Zhou, J. Yu, M. Jaroniec, All-solid-state Z-scheme photocatalytic systems, *Adv. Mater.* 26 (2014) 4920–4935.

[16] J. Jin, J. Yu, D. Guo, C. Cui, W. Ho, A hierarchical Z-scheme CdS-WO<sub>3</sub> photocatalyst with enhanced CO<sub>2</sub> reduction activity, *Small* 11 (2015) 5262–5271.

[17] D. Xu, B. Cheng, S. Cao, J. Yu, Enhanced photocatalytic activity and stability of Z-scheme Ag<sub>2</sub>CrO<sub>4</sub>-GO composite photocatalysts for organic pollutant degradation, *Appl. Catal. B: Environ.* 164 (2015) 380–388.

[18] Z. Pan, T. Hisatomi, Q. Wang, S. Chen, M. Nakabayashi, N. Shibata, C. Pan, T. Takata, M. Katayama, T. Minegishi, Photocatalyst sheets composed of particulate LaMg<sub>1/3</sub>Ta<sub>2/3</sub>O<sub>2</sub>N and Mo-doped BiVO<sub>4</sub> for Z-scheme water splitting under visible light, *ACS Catal.* 6 (2016) 7188–7196.

[19] J. Low, C. Jiang, B. Cheng, S. Wageh, A.A. Al-Ghamdi, J. Yu, A review of direct Z-scheme photocatalysts, *Small Methods* 1 (2017) 1700080.

[20] X. Wang, K. Maeda, A. Thomas, K. Takanabe, G. Xin, J.M. Carlsson, K. Domen, M. Antonietti, A metal-free polymeric photocatalyst for hydrogen production from water under visible light, *Nat. Mater.* 8 (2009) 76–80.

[21] J. Ran, T.Y. Ma, G. Gao, X.-W. Du, S.Z. Qiao, Porous P-doped graphitic carbon nitride nanosheets for synergistically enhanced visible-light photocatalytic H<sub>2</sub> production, *Energy Environ. Sci.* 8 (2015) 3708–3717.

[22] S. Cao, J. Low, J. Yu, M. Jaroniec, Polymeric photocatalysts based on graphitic carbon nitride, *Adv. Mater.* 27 (2015) 2150–2176.

[23] Y. Zheng, L. Lin, B. Wang, X. Wang, Graphitic carbon nitride polymers toward sustainable photoredox catalysis, *Angew. Chem. Int. Ed.* 54 (2015) 12868–12884.

[24] K. Wang, Q. Li, B. Liu, B. Cheng, W. Ho, J. Yu, Sulfur-doped g-C<sub>3</sub>N<sub>4</sub> with enhanced photocatalytic CO<sub>2</sub>-reduction performance, *Appl. Catal. B: Environ.* 176–177 (2015) 44–52.

[25] W.-J. Ong, L.-L. Tan, Y.H. Ng, S.-T. Yong, S.-P. Chai, Graphitic carbon nitride (g-C<sub>3</sub>N<sub>4</sub>)-based photocatalysts for artificial photosynthesis and environmental remediation: are we a step closer to achieving sustainability? *Chem. Rev.* 116 (12) (2016) 7159–7329.

[26] P. Xia, B. Zhu, J. Yu, S. Cao, M. Jaroniec, Ultra-thin nanosheet assemblies of graphitic carbon nitride for enhanced photocatalytic CO<sub>2</sub> reduction, *J. Mater. Chem. A* 5 (2017) 3230–3238.

[27] J. Yu, S. Wang, J. Low, W. Xiao, Enhanced photocatalytic performance of direct Z-scheme g-C<sub>3</sub>N<sub>4</sub>-TiO<sub>2</sub> photocatalysts for the decomposition of formaldehyde in air, *Phys. Chem. Chem. Phys.* 15 (2013) 16883–16890.

[28] D.J. Martin, P.J.T. Reardon, S.J.A. Moniz, J. Tang, Visible light-driven pure water splitting by a nature-inspired organic semiconductor-based system, *J. Am. Chem. Soc.* 136 (2014) 12568–12571.

[29] W. Yu, D. Xu, T. Peng, Enhanced photocatalytic activity of g-C<sub>3</sub>N<sub>4</sub> for selective CO<sub>2</sub> reduction to CH<sub>3</sub>OH via facile coupling of ZnO: a direct Z-scheme mechanism, *J. Mater. Chem. A* 3 (2015) 19936–19947.

[30] J. Wen, J. Xie, X. Chen, X. Li, A review on g-C<sub>3</sub>N<sub>4</sub>-based photocatalysts, *Appl. Surf. Sci.* 391 (2017) 72–123.

[31] J. Li, M. Zhang, Q. Li, J. Yang, Enhanced visible light activity on direct contact Z-scheme g-C<sub>3</sub>N<sub>4</sub>-TiO<sub>2</sub> photocatalyst, *Appl. Surf. Sci.* 391 (2017) 184–193.

[32] K. Sivula, F.L. Formal, M. Grätzel, WO<sub>3</sub>-Fe<sub>2</sub>O<sub>3</sub> photoanodes for water splitting: a host scaffold, guest absorber approach, *Chem. Mater.* 21 (2009) 2862–2867.

[33] M. Stefk, M. Cornuz, N. Mathews, T. Hisatomi, S. Mhaisalkar, M. Grätzel, Transparent, conducting Nb SnO<sub>2</sub> for host–guest photoelectrochemistry, *Nano Lett.* 12 (2012) 5431–5435.

[34] I. Kondofersky, H.K. Dunn, A. Müller, B. Mandlmeier, J.M. Feckl, D. Fattakhova-Rohlfing, C. Scheu, L.M. Peter, T. Bein, Electron collection in host–guest nanostructured hematite photoanodes for water splitting: the influence of scaffold doping density, *ACS Appl. Mater. Interfaces* 7 (2015) 4623–4630.

[35] H. Katsumata, Y. Tachi, T. Suzuki, S. Kaneko, Z-scheme photocatalytic hydrogen production over WO<sub>3</sub>/g-C<sub>3</sub>N<sub>4</sub> composite photocatalysts, *RSC Adv.* 4 (2014) 21405–21409.

[36] L. Cui, X. Ding, Y. Wang, H. Shi, L. Huang, Y. Zuo, S. Kang, Facile preparation of Z-scheme WO<sub>3</sub>/g-C<sub>3</sub>N<sub>4</sub> composite photocatalyst with enhanced photocatalytic performance under visible light, *Appl. Surf. Sci.* 391 (2017) 202–210.

[37] K. Kailasam, A. Fischer, G. Zhang, J. Zhang, M. Schwarze, M. Schröder, X. Wang, R. Schomäcker, A. Thomas, Mesoporous carbon nitride-tungsten oxide composites for enhanced photocatalytic hydrogen evolution, *ChemSusChem* 8 (2015) 1404–1410.

[38] X. Liu, A. Jin, Y. Jia, T. Xia, C. Deng, M. Zhu, C. Chen, X. Chen, Synergy of adsorption and visible-light photocatalytic degradation of methylene blue by a bifunctional Z-scheme heterojunction of WO<sub>3</sub>/g-C<sub>3</sub>N<sub>4</sub>, *Appl. Surf. Sci.* 405 (2017) 359–371.

[39] J.Y. Zheng, G. Song, J. Hong, T.K. Van, A.U. Pawar, D.Y. Kim, C.W. Kim, Z. Haider, Y.S. Kang, Facile fabrication of WO<sub>3</sub> nanoplates thin films with dominant crystal facet of (002) for water splitting, *Crystal Growth Des* 14 (2014) 6057–6066.

[40] J. Lee, H.S. Shim, M. Lee, J.K. Song, D. Lee, Size-controlled electron transfer and photocatalytic activity of ZnO–Au nanoparticle composites, *J. Phys. Chem. Lett.* 2 (2011) 2840–2845.

[41] K. Tvrđ, P.A. Frantsuzov, P.V. Kamat, Photoinduced electron transfer from semiconductor quantum dots to metal oxide nanoparticles, *Proc. Natl. Acad. Sci.* 108 (2011) 29–34.

[42] G. Paolo, B. Stefano, B. Nicola, C. Matteo, C. Roberto, C. Carlo, C. Davide, L.C. Guido, C. Matteo, D. Ismaila, C. Andrea Dal, G. Stefano de, F. Stefano, F. Guido, G. Ralph, G. Uwe, G. Christos, K. Anton, L. Michele, M.-S. Layla, M. Nicola, M. Francesco, M. Riccardo, P. Stefano, P. Alfredo, P. Lorenzo, S. Carlo, S. Sandro, S. Gabriele, P.S. Ari, S. Alexander, U. Paolo, M.W. Renata, QUANTUM ESPRESSO: a modular and open-source software project for quantum simulations of materials, *J. Phys.: Condens. Matter* 21 (2009) 395502.

[43] Y. Cui, Z. Ding, X. Fu, X. Wang, Construction of conjugated carbon nitride nanoarchitectures in solution at low temperatures for photoredox catalysis, *Angew. Chem. Int. Ed.* 51 (2012) 11814–11818.

[44] P. Yang, J. Zhao, J. Wang, B. Cao, L. Li, Z. Zhu, Construction of Z-scheme carbon nanodots/WO<sub>3</sub> with highly enhanced photocatalytic hydrogen production, *J. Mater. Chem. A* 3 (2015) 8256–8259.

[45] J.C. Meyer, C. Kisielowski, R. Erni, M.D. Rossell, M.F. Crommie, A. Zettl, Direct imaging of lattice atoms and topological defects in graphene membranes, *Nano Lett.* 8 (2008) 3582–3586.

[46] C. Huang, C. Chen, M. Zhang, L. Lin, X. Ye, S. Lin, M. Antonietti, X. Wang, Carbon-doped BN nanosheets for metal-free photoredox catalysis, *Nat. Commun.* 6 (2015) 7698.

[47] Y. Kang, Y. Yang, L.C. Yin, X. Kang, G. Liu, H.M. Cheng, An amorphous carbon nitride photocatalyst with greatly extended visible-light-responsive range for photocatalytic hydrogen generation, *Adv. Mater.* 27 (2015) 4572–4577.

[48] C.F. Fu, Q. Luo, X. Li, J. Yang, Two-dimensional van der Waals nanocomposites as Z-scheme type photocatalysts for hydrogen production from overall water splitting, *J. Mater. Chem. A* 4 (2016) 18892–18898.

[49] R.H. Coridan, M. Shaner, C. Wiggenhorn, B.S. Brunschwig, N.S. Lewis, Electrical and photoelectrochemical properties of WO<sub>3</sub>/Si tandem photoelectrodes, *J. Phys. Chem. C* 117 (2013) 6949–6957.

[50] B. Zhu, J. Zhang, C. Jiang, B. Cheng, J. Yu, First principle investigation of halogen-doped monolayer g-C<sub>3</sub>N<sub>4</sub> photocatalyst, *Appl. Catal. B: Environ.* 207 (2017) 27–34.

[51] J. Liu, B. Cheng, J. Yu, A new understanding of the photocatalytic mechanism of the direct Z-scheme g-C<sub>3</sub>N<sub>4</sub>/TiO<sub>2</sub> heterostructure, *Phys. Chem. Chem. Phys.* 18 (2016) 31175–31183.

[52] J. Zhang, P. Zhou, J. Liu, J. Yu, New understanding of the difference of photocatalytic activity among anatase, rutile and brookite TiO<sub>2</sub>, *Phys. Chem. Chem. Phys.* 16 (2014) 20382–20386.

[53] J. Zhang, S. Wageh, A. Al-Ghamdi, J. Yu, New understanding on the different photocatalytic activity of wurtzite and zinc-blende CdS, *Appl. Catal. B: Environ.* 192 (2016) 101–107.

[54] H. Zhang, L. Liu, Z. Zhou, Towards better photocatalysts: first-principles studies of the alloying effects on the photocatalytic activities of bismuth oxyhalides under visible light, *Phys. Chem. Chem. Phys.* 14 (2012) 1286–1292.

[55] W. Yu, J. Zhang, T. Peng, New insight into the enhanced photocatalytic activity of N-, C- and S-doped ZnO photocatalysts, *Appl. Catal. B: Environ.* 181 (2016) 220–227.